ACCSCIENCE PUBLISHING

Advances in Radiotherapy & Nuclear Medicine

ORIGINAL RESEARCH ARTICLE

A commissioning workflow for quantitative ^{177}Lu SPECT/CT across different Siemens scanner–reconstruction configurations

Leonardo Lampertico[1,2], Gaia Muti[2*], Claudia Carbonini[2], Chiara Romanò[2], Antonio Scarale[3], Claudio Rossetti[3], and Paola Enrica Colombo[2]

[1]Physics Department, Faculty of Physics, University of Milan, Milan, Lombardy, Italy

[2]Medical Physics Department, ASST GOM Niguarda, Milan, Lombardy, Italy

[3]Nuclear Medicine Department, ASST GOM Niguarda, Milan, Lombardy, Italy

Abstract

The accuracy of quantitative lutetium-177 single-photon emission computed tomography/computed tomography (^{177}Lu SPECT/CT) depends on the imaging system, acquisition protocol, reconstruction algorithm, and calibration strategy. This study aimed to develop and evaluate a practical commissioning workflow to optimize ^{177}Lu imaging across different commercial scanner–reconstruction configurations. Three Siemens workflows were evaluated: FLASH3D and xSPECT Quant on the Symbia Intevo Bold, and FLASH3D+ on the Symbia Pro.specta. A uniform phantom was used to assess image noise and derive calibration factors for the ordered-subset expectation maximization (OSEM)-based reconstructions. Recovery coefficients (RCs) were evaluated via an International Electrotechnical Commission/National Electrical Manufacturers Association phantom at various sphere-to-background ratios and modeled using a three-parameter logistic function for partial volume correction. Reconstruction parameters were optimized by jointly evaluating RC convergence and image noise, followed by quantitative validation using an anthropomorphic phantom. OSEM-based workflows showed a predictable dependence on equivalent iterations, yielding lower image noise. Conversely, xSPECT Quant exhibited complex parameter dependence and higher noise, but provided superior activity recovery—with RCs closer to unity—and the lowest quantification errors during validation. A reconstruction setting of two subsets and 30 iterations was selected for all workflows. For FLASH3D and FLASH3D+, this configuration provided RCs closest to unity while maintaining the coefficient of variation below the predefined 15% threshold. The same setting was adopted for xSPECT Quant to ensure methodological consistency despite its intrinsically higher image noise. This commissioning workflow provides a practical framework for local ^{177}Lu SPECT/CT optimization. Among the configurations, xSPECT Quant yielded higher recovery coefficients and lower quantification errors, albeit with increased noise. These findings highlight the need for locally optimized protocols for patient-specific dosimetry and do not establish the general superiority of any one reconstruction algorithm.

Keywords: Lutetium-177 single-photon emission computed tomography/computed tomography; Quantitative imaging; Recovery coefficients; Reconstruction algorithms; xSPECT Quant; Ordered-subset expectation maximization reconstruction; Calibration; Internal dosimetry

***Corresponding author:**
Gaia Muti
(gaia.muti@ospedaleniguarda.it)

Citation: Lampertico L, Muti G, Carbonini C, *et al*. A commissioning workflow for quantitative ^{177}Lu SPECT/CT across different Siemens scanner–reconstruction configurations. *Adv Radiother Nucl Med.* 2026;4(3):026260029. doi: 10.36922/ARNM026260029

Received: June 26, 2026

Revised: July 20, 2026

Accepted: July 30, 2026

Published online: August 20, 2026

Copyright: © 2026 Author(s). This is an Open-Access article distributed under the terms of the Creative Commons Attribution License, permitting distribution, and reproduction in any medium, provided the original work is properly cited.

Publisher's Note: AccScience Publishing remains neutral with regard to jurisdictional claims in published maps and institutional affiliations.

1. Introduction

Radiopharmaceutical therapy has become a fundamental component of precision oncology, allowing the selective delivery of ionizing radiation to malignant tissues while minimizing irradiation of surrounding healthy organs. The concept of theragnostics, which combines molecular imaging and targeted radionuclide therapy using the same biological pathway, has significantly expanded the clinical applications of nuclear medicine over the last few decades.[1-3]

Among the available therapeutic radionuclides, Lutetium-177 (^{177}Lu) has emerged as one of the most successful due to its favorable physical characteristics, including medium-energy beta emissions suitable for therapy and gamma emissions that enable post-treatment imaging and dosimetric evaluation.[4] The development of peptide receptor radionuclide therapy using radiolabeled somatostatin analogs represented a major advancement for the treatment of neuroendocrine tumors. Early clinical experiences with 90Y-labeled compounds demonstrated the feasibility of targeted radionuclide treatment[5], while subsequent studies with ^{177}Lu-1,4,7,10-tetraazacyclododecane-1,4,7,10-tetraacetic acid (DOTA)-based compounds reported improved therapeutic efficacy and favorable toxicity profiles.[6-8] The efficacy of ^{177}Lu-DOTA-(Tyr^3)-octreotate was demonstrated by the phase III NETTER-1 trial, which showed a significant improvement in progression-free survival for patients with advanced midgut neuroendocrine tumors.[9] Final overall survival results further confirmed its long-term clinical benefit.[10]

In parallel, the development of prostate-specific membrane antigen (PSMA)-targeted radioligands has extended the use of ^{177}Lu therapy to metastatic castration-resistant prostate cancer. Preclinical and clinical investigations of PSMA-617 demonstrated high tumor affinity and favorable biodistribution, leading to successful therapeutic applications and ultimately to the establishment of ^{177}Lu-PSMA-617 as a standard therapeutic option for selected patients.[11-14]

The increasing clinical implementation of ^{177}Lu-based therapies has highlighted the need to move beyond fixed administered activities toward individualized treatment planning based on patient-specific absorbed dose estimation.[15-17] Personalized dosimetry requires accurate determination of the three-dimensional (3D) activity distribution over time, making quantitative single-photon emission computed tomography/computed tomography (SPECT/CT) an essential tool for treatment optimization and therapy monitoring.[18-23]

However, accurate activity quantification in SPECT imaging remains challenging due to several physical and technical factors affecting image formation. Photon attenuation, Compton scatter, finite collimator–detector response (CDR), limited spatial resolution, image noise, and partial volume effects can all introduce significant errors in reconstructed activity concentrations.[24,25] The implementation of advanced correction methods, including attenuation correction, scatter correction, and resolution recovery, has considerably improved quantitative SPECT performance.[26,27]

A critical aspect of quantitative SPECT imaging is the correction of partial volume effects, particularly for small lesions and structures with complex geometries. Due to the limited spatial resolution of SPECT systems, measured activity concentrations may significantly underestimate true values. Recovery coefficient (RC)-based correction approaches have therefore been widely investigated and remain an essential component of quantitative dosimetry workflows.[28,29]

Reliable quantitative imaging also requires accurate system calibration and validation. Several studies have investigated calibration factor (CF) determination and the optimization of quantitative SPECT protocols for ^{177}Lu imaging, demonstrating that acquisition parameters, reconstruction methods, and correction strategies influence quantitative accuracy.[30-39]

Among the different reconstruction approaches, iterative algorithms based on ordered-subset expectation maximization (OSEM) have become the standard for clinical SPECT reconstruction due to their ability to incorporate physical correction models and improve image quality. More recently, dedicated quantitative reconstruction algorithms, such as xSPECT Quant based on the ordered subset conjugate gradient (OSCG) method, have been introduced to further improve absolute activity recovery and quantitative accuracy.[40] Nevertheless, these advanced reconstruction methods may exhibit different convergence properties and noise behavior compared with conventional OSEM-based algorithms, requiring dedicated optimization and validation before routine clinical implementation.

Therefore, the aim of this study was to perform a comprehensive comparison of three commercial quantitative ^{177}Lu SPECT/CT imaging workflows: FLASH3D and xSPECT Quant implemented on the Symbia Intevo Bold, and FLASH3D+ implemented on the Symbia Pro.specta. Their quantitative performance was assessed using phantom measurements with known activity concentrations by analyzing image noise, calibration-

factor stability, RCs, and the accuracy of absolute activity quantification. The final objective was to establish an optimized and clinically applicable commissioning workflow for accurate quantitative ^{177}Lu SPECT/CT imaging and patient-specific dosimetry.

2. Materials and methods

2.1. SPECT/CT systems and acquisition protocols

Two SPECT/CT systems were included in this study: the Symbia Intevo Bold and the Symbia Pro.specta. Both systems are hybrid imaging platforms integrating SPECT and CT technologies, allowing accurate anatomical co-registration and CT-based attenuation correction for quantitative imaging.

To ensure consistency and comparability across measurements and reconstruction protocols, a standardized acquisition protocol was adopted for both systems. SPECT acquisitions were performed in step-and-shoot mode using 36 projections over a complete 360° rotation, with an acquisition time of 20 s per projection. Medium-energy low-penetration collimators were employed, as they provided an appropriate balance between system sensitivity and septal penetration for ^{177}Lu imaging, considering its characteristic gamma emission spectrum.

The SPECT energy acquisition was centered on the 208 keV photopeak, corresponding to the main gamma emission of ^{177}Lu, using an energy window with a width of 20%. In addition, two adjacent scatter correction windows were positioned below and above the photopeak window, each with a width corresponding to 10% of the main energy window. CT acquisitions were performed according to standard clinical protocols and were used for attenuation correction and anatomical localization.

2.2. Reconstruction algorithms

Three Siemens reconstruction algorithms were evaluated: FLASH3D, FLASH3D+, and xSPECT Quant.

FLASH3D was a conventional clinical 3D-OSEM reconstruction algorithm that iteratively estimated the activity distribution by minimizing the discrepancy between measured projection data and forward-projected estimates. FLASH3D+ built upon the same iterative reconstruction framework while incorporating an enhanced modeling of the CDR to improve spatial resolution and quantitative accuracy.

(i) Resolution recovery

Both algorithms incorporated a 3D, distance-dependent model of the CDR to compensate for the spatial resolution degradation caused by geometric blurring and photon penetration through the collimator septa. FLASH3D+ employed a more accurate CDR model than the conventional FLASH3D implementation, providing improved point spread function modeling, particularly for sources located farther from the collimator. This enhanced resolution recovery improved spatial resolution, lesion contrast, and RCs while preserving image noise characteristics.

(ii) Physical corrections

Both algorithms compensated for photon attenuation using a CT-derived attenuation map (μ-map), generated by converting CT Hounsfield units into linear attenuation coefficients at the selected ^{177}Lu photopeak (208 keV) through bilinear scaling. Scatter correction was performed using the triple energy window (TEW) method, in which scatter estimates derived from adjacent lower and upper energy windows were subtracted from the primary photopeak projections before iterative reconstruction.

(iii) Output units and calibration

By default, the reconstructed voxel values produced by FLASH3D and FLASH3D+ were proportional to the detected photon counts and therefore did not directly represent absolute activity concentration. Quantitative imaging required calibration of the imaging system using a scanner-specific CF, typically determined from phantom measurements with a known ^{177}Lu activity concentration. Once calibrated, reconstructed voxel values could be converted into absolute activity concentration (Bq/mL), enabling quantitative SPECT imaging.

xSPECT Quant was Siemens Healthineers' quantitative SPECT reconstruction algorithm based on an OSCG optimization framework.[40] Unlike conventional OSEM-based approaches, xSPECT performed reconstruction directly on the high-resolution CT voxel grid, ensuring precise spatial correspondence between anatomical and functional information throughout the iterative reconstruction process.

(i) Resolution recovery and system modeling

xSPECT Quant employed a highly detailed voxel-based system model that accurately described the imaging geometry of the collimator–detector system. The system matrix incorporated distance-dependent collimator response together with detector characteristics, allowing a more accurate forward projection than conventional analytical models. By combining this detailed physical modeling with reconstruction on the CT matrix, xSPECT Quant improved spatial resolution, contrast recovery, and quantitative accuracy, particularly for small structures.

(ii) Physical corrections
Attenuation correction based on the CT-derived μ-map and scatter correction using the TEW method were incorporated directly into the iterative reconstruction process. The reconstruction framework also included comprehensive modeling of the CDR, accounting for distance-dependent resolution degradation and photon penetration effects relevant to ^{177}Lu imaging.

(iii) Output units and quantitative calibration
xSPECT Quant was designed to provide reconstructed images directly in quantitative units, such as activity concentration (Bq/mL). Absolute quantification was achieved through a scanner-specific calibration performed during system commissioning and quality assurance procedures. The corresponding system sensitivity was automatically incorporated into the reconstruction workflow, eliminating the need for manual post-reconstruction scaling by the user. Consequently, reconstructed voxel values were directly proportional to the true radionuclide activity distribution, facilitating quantitative dosimetry.

2.3. Calibration and reconstruction optimization workflow

All ^{177}Lu activities were measured using the institutional dose calibrator ISOMED 2010 (ELSE Solution, Italy). To determine the calibrator's CF, a vial containing a certified activity with a 5% uncertainty, which was not traceable to the National Institute of Standards and Technology, was used. Subsequently, a syringe geometry CF was also determined based on the difference in activity subtracted from the vial with the certified activity. The syringe geometry CF was used to prepare all the activity for the phantoms.

For the absolute calibration of the xSPECT Quant reconstruction algorithm, a local calibration procedure was adopted to ensure consistency between the activity measurements used in clinical practice and the quantitative SPECT images. The point source was positioned in air at the SPECT/CT isocenter and acquired according to the manufacturer's point-source calibration protocol.

The activity measured with the local dose calibrator was then used as the reference input for the Siemens calibration software, which determined the system sensitivity for the specific scanner, collimator, and radionuclide configuration. This sensitivity factor, expressed in counts per second per megabecquerel (cps/MBq), was automatically incorporated within the quantitative reconstruction framework of xSPECT Quant. Consequently, reconstructed voxel values were directly expressed in absolute activity concentration units (Bq/mL), without requiring any user-defined post-reconstruction CF. This procedure effectively established a calibration between the SPECT/CT system and the local dose calibrator, ensuring that quantitative activity estimates derived from reconstructed images remained consistent with the activity measurements used throughout the clinical dosimetry workflow. Conversely, for the non-quantitative FLASH3D and FLASH3D+ reconstructions, CFs were experimentally derived from a uniform phantom with known activity concentration to convert reconstructed counts into absolute activity values.

A systematic optimization of reconstruction parameters was performed by varying subsets and iterations over a wide range. For FLASH3D and FLASH3D+, subsets from 1 to 18 (1, 2, 3, 4, 6, 8, 9, 12, and 18) and iterations from 1 to 90 (1, 3, 5, 10, 15, 30, 45, 60, 75, and 90) were investigated. Reconstruction settings were characterized in terms of equivalent iterations (EI), defined as:

$$\mathrm{EI} = \mathrm{subsets} \times \mathrm{iterations} \quad (1)$$

For each reconstruction setting, image noise and calibration stability were evaluated using the uniform phantom. For xSPECT Quant[41], only subsets 1 through 4 were evaluated, and the analysis was restricted to image noise, as absolute calibration was intrinsically provided by the reconstruction algorithm. No post-reconstruction Gaussian filtering was applied to avoid smoothing effects that could influence quantitative measurements and RC estimation.

Recovery coefficients were subsequently evaluated using the International Electrotechnical Commission National Electrical Manufacturers Association (IEC NEMA) body phantom containing spherical inserts with different inner radii (57, 37, 28, 22, 17, 13, and 10 mm) and sphere-to-background activity concentration ratios.[42] For the xSPECT Quant workflow, the RC analysis was restricted to subsets 1 and 2. Together with the previously assessed image noise behavior, the RC analysis was used to guide the selection of the optimal reconstruction parameters.

The reconstruction parameters selected through this optimization procedure were then adopted for the final quantitative validation using an anthropomorphic torso phantom containing inserts with known activity concentrations. The derived CFs and RC corrections were applied to estimate activity concentrations, which were subsequently compared with the corresponding reference values. A schematic overview of the complete workflow is reported in Figure 1. This procedure enabled a comprehensive assessment of the quantitative imaging chain, from system calibration and reconstruction optimization to final validation, providing the basis for subsequent patient-specific dosimetric applications in ^{177}Lu therapy.

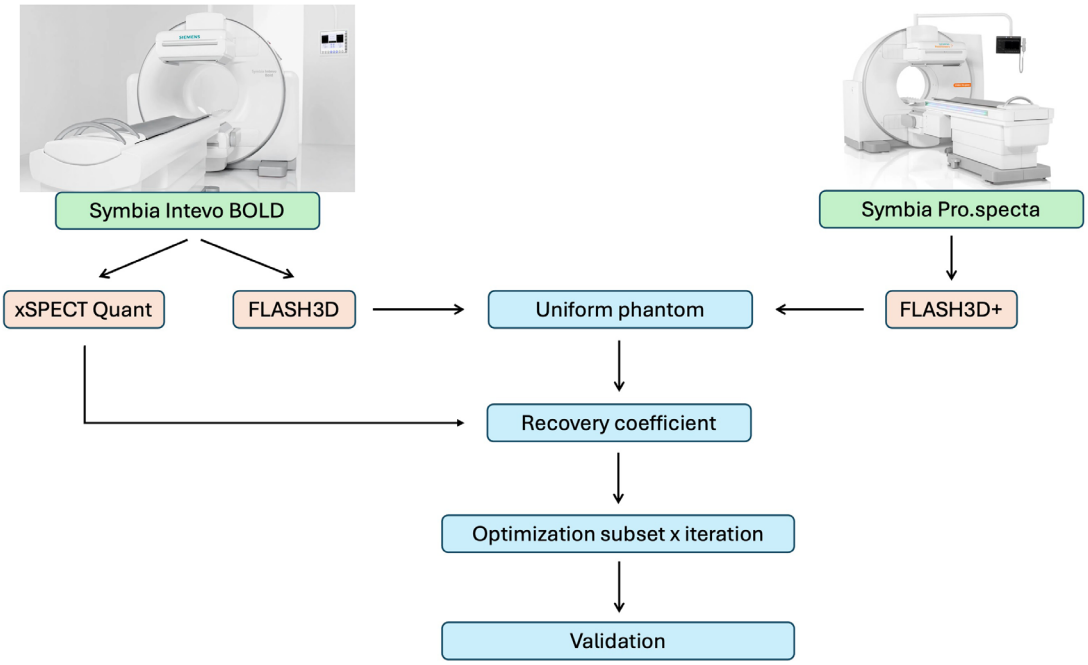

Figure 1. Schematic representation of the quantitative calibration and reconstruction optimization workflow for the two SPECT/CT systems. For the Symbia Intevo Bold system, both xSPECT Quant and FLASH3D reconstruction protocols are considered, whereas the Symbia Pro.specta system employs the FLASH3D+ algorithm. Calibration factors are derived for non-quantitative reconstructions. Noise and recovery coefficients are used to guide the optimization of reconstruction parameters in terms of subsets and iterations. The optimized configuration is subsequently validated using an anthropomorphic phantom.
Abbreviation: SPECT/CT: single-photon emission computed tomography/computed tomography.

2.4. Phantoms

Three different phantoms were used in this study. All phantoms were acquired using the same SPECT/CT acquisition protocol described in the previous section.

(i) Uniform phantom: The uniform phantom had a total volume of 5,380 mL and was filled with a known activity of 700 MBq of ^{177}Lu, ensuring a homogeneous activity distribution throughout the volume. The uniform phantom was reconstructed using all three available reconstruction algorithms: FLASH3D, FLASH3D+, and xSPECT Quant. For the non-quantitative reconstruction protocols, the uniform phantom was used to determine CFs by relating reconstructed image counts to the known activity concentration. In addition, image noise was evaluated in order to assess the impact of reconstruction parameters on quantitative stability. For the quantitative xSPECT Quant protocol, the uniform phantom was used exclusively to evaluate image noise as a function of reconstruction settings, since absolute calibration was already provided by the system through the point source calibration procedure.

(ii) International Electrotechnical Commission NEMA body phantom: The IEC NEMA body phantom was used to evaluate the effect of background activity on RC. The phantom had a total volume of 9,820 mL, excluding a lung insert. The background volume was calculated as the total volume minus the volume of the spheres, resulting in 9,675 mL. In addition to the six standard spheres, an additional larger sphere with a diameter of 57 mm was inserted into the phantom to extend the range of lesion sizes investigated. This larger sphere was also used for coefficient of variation (COV) assessment within a lesion-like insert. All spheres were filled with the same activity concentration, ensuring uniform uptake within the lesions. The phantom was acquired under four different sphere-to-background activity concentration ratios, obtained by varying the background activity concentration: cold background, 15:1, 10:1, and 5:1. This experimental design was adopted to investigate the dependence of RCs on different sphere-to-background ratios, following the approach proposed by Raskin *et al.*[37], who demonstrated that RC is strongly influenced by background activity levels. This aspect is particularly relevant in clinical ^{177}Lu dosimetry, where lesions may be located in regions with markedly different

background conditions. For example, liver metastases are typically embedded in high-uptake background tissue, whereas bone metastases in peripheral skeletal regions may be surrounded by low or negligible background activity. Therefore, understanding how RC varies as a function of background conditions is essential to ensure accurate activity quantification across different clinical scenarios.

(iii) Anthropomorphic torso phantom: An anthropomorphic torso phantom was used as the final validation step of the calibration and quantification workflow. The phantom had a total volume of 9,600 mL and was filled with an overall activity of 460 MBq of ^{177}Lu. Three inserts with different geometries were included: a spherical insert with a diameter of 34 mm and a volume of 20.6 mL, a kidney-shaped insert with a volume of 106 mL, and a heart-shaped insert with a volume of 115 mL. All inserts were filled with the same activity concentration. The spherical insert was placed in a cold background region, corresponding to a liver compartment of the phantom filled only with water. The kidney and heart inserts were instead placed in a background with an activity concentration ratio of approximately 10:1 with respect to the inserts. The anthropomorphic phantom was acquired and reconstructed using all three reconstruction algorithms (FLASH3D, FLASH3D+, and xSPECT Quant) in order to validate the full quantification chain. Since the true activity concentration of each insert was known, the reconstructed images were converted from counts to activity concentration using the previously determined CF for the non-quantitative protocols. Subsequently, the appropriate RCs were applied according to the corresponding background conditions: a cold background RC was used for the spherical insert, while a 10:1 sphere-to-background ratio RC was applied for the kidney and heart inserts. This procedure allowed the estimation of the measured activity concentration for each insert, which was then compared with the known reference values. The percentage deviation between measured and true activity was calculated in order to assess the accuracy of each reconstruction protocol and to quantify the overall uncertainty of the calibration workflow.

2.5. Quantitative analysis

The quantitative analysis framework adopted in this study was based on the formalism described by Mezzenga *et al.*[36] The equations and definitions reported in this section were implemented according to the methodology proposed in that work and adapted to the specific acquisition and reconstruction protocols investigated in this study.

Image noise was expressed as the COV. According to IEC guidelines, within the uniform phantom the COV was calculated over a region of interest corresponding to approximately 80% of the phantom volume in order to avoid edge effects and partial volume artifacts, whereas within the IEC NEMA phantom, the COV was calculated over a region of interest defined inside the largest sphere. The COV was defined as:

$$COV(EI)\% = 100 \cdot \frac{\sigma(EI)}{M(EI)} \tag{2}$$

where σ(EI) and M(EI) represent the standard deviation and mean voxel value within the selected VOI, respectively.[36]

For non-quantitative reconstructions (FLASH3D and FLASH3D+), the CF expressed the relationship between reconstructed counts and known activity concentration. To account for the impact of algorithm convergence, the CF was calculated for each specific reconstruction setting as:

$$CF(EI) = \frac{C(EI)/T}{V_{VOI} \cdot c} \tag{3}$$

where the CF unit is expressed in cps/MBq. In this formulation, *C(EI)* represents the raw (non-decay-corrected) total counts extracted from the volume of interest (VOI), and *T* is the acquisition duration, which was equal to 720 seconds, thereby converting the reconstructed counts into a count rate in counts per second (cps).

The VOI was defined to ensure statistical robustness and eliminate edge effects: it was positioned fully within the dimensions of the uniform phantom (1 cm within the outer contour of the phantom) and excluded the 10% end-planes at each side of the axial field of view (FOV), thus remaining strictly within the central 80% of the axial FOV.

The term V_{VOI} represents the volume of this specific VOI (in mL), while *c* is the true activity concentration inside the phantom (expressed in MBq/mL). To ensure absolute accuracy, the concentration *c* was determined using the certified internal volume of the uniform phantom and the net ^{177}Lu activity (calculated by subtracting the post-injection residual syringe activity from the initial pre-injection measurement using the institutional dose calibrator). Crucially, this net activity was decay-corrected using the physical half-life of ^{177}Lu (6.647 days) to the exact midpoint of the SPECT acquisition. Camera dead-time was verified via system logs to be negligible (<1%) under these clinical-range activities, and the dose calibrator accuracy was maintained through standard daily quality control checks.

The quantitative accuracy of activity recovery was evaluated using the IEC NEMA body phantom. The RC was defined for each sphere as:

$$RC(EI) = \frac{C(EI)}{V \cdot CF(EI) \cdot c} \tag{4}$$

where C(EI) is the total reconstructed counts within the CT-based contour of the sphere, V is the corresponding sphere volume, CF(EI) is the CF associated with the reference configuration, and c is the true activity concentration. For xSPECT Quant, RCs were directly obtained as the ratio between measured and true activity concentration:

$$RC(EI) = \frac{C_{meas}(EI)}{C_{true}} \tag{5}$$

where C_{meas}(EI) is the reconstructed activity concentration within the sphere, and C_{true} is the corresponding true activity concentration. Final validation of the quantification workflow was performed using an anthropomorphic torso phantom with inserts of known activity concentration. The percentage deviation between measured and true activity was calculated as:

$$D = 100 \cdot \frac{A_R(EI) - A_T}{A_T} \tag{6}$$

where A_R(EI) is the reconstructed activity, and A_T is the true reference activity.

3. Results

The quantitative performance of the investigated reconstruction algorithms was evaluated through image noise analysis, CF stability, and RC assessment. The results are reported separately for the different reconstruction methods and SPECT/CT systems.

3.1. Coefficient of variation analysis

The image noise was evaluated in terms of the COV using both the uniform phantom and the largest sphere of the IEC NEMA body phantom, for all acquisitions and sphere-to-background activity concentration ratios.

For the Symbia Pro.specta system, the COV depended primarily on the EI value. In particular, for a given EI value, comparable COV values were observed regardless of the specific combination of subsets and iterations, indicating that noise behavior was predominantly governed by EI. The COV as a function of EI for all phantom configurations is summarized in Figure 2.

In the uniform phantom, the COV exhibited a minimum at EI = 6, followed by a monotonic increase with increasing EI. For higher EI values, image noise progressively increased, reaching approximately 12% at EI = 60.

A different behavior was observed for the largest sphere in the IEC NEMA phantom. In the case of a cold background, the COV showed a local maximum for EI values between 9 and 12, with a value of approximately 43%. This was followed by a decrease toward a local minimum at EI ≈ 80–90, corresponding to a COV of about 32%. For higher EI values, the COV increased again monotonically. For acquisitions with non-zero background activity, a similar trend was observed, with variations in absolute COV values depending on the sphere-to-background ratio. For a 15:1 ratio, the local maximum decreased to approximately 39%, while the minimum increased to about 34%, occurring at comparable EI values. A similar behavior was found for the 10:1 ratio, with a maximum COV of approximately 39% at EI = 9–12 and a minimum of about 34% at EI ≈ 80–90. For the 5:1 ratio, both the maximum and minimum COV values were reduced, reaching approximately 32% and 31%, respectively, while maintaining the same qualitative trend as a function of EI.

Overall, these results indicated that image noise in the Symbia Pro.specta system was strongly dependent on the EI value, with distinct behaviors observed between uniform and non-uniform activity distributions, and a clear influence of background activity on noise levels in lesion-like structures.

For the Symbia Intevo Bold system, two reconstruction algorithms were analyzed: the non-quantitative FLASH3D and the quantitative xSPECT Quant.

For the FLASH3D algorithm, the behavior of the COV was consistent with that observed for the Symbia Pro. specta system, as shown in Figure 3. In particular, the COV primarily depended on EI, with similar values obtained for different combinations of subsets and iterations yielding the same EI. Both the uniform phantom and the IEC NEMA phantom (largest sphere) exhibited the same qualitative trends described previously, with slightly higher absolute noise levels. For example, in the uniform phantom at EI = 60, the COV increased from approximately 12% for the Symbia Pro.specta system to about 13% for the Symbia Intevo Bold. Similarly, in the IEC NEMA phantom, COV values were consistently higher by a few percentage points across all sphere-to-background ratios, while preserving the same overall behavior. This was consistent with expectations, as both FLASH3D and FLASH3D+ were based on 3D OSEM reconstruction.

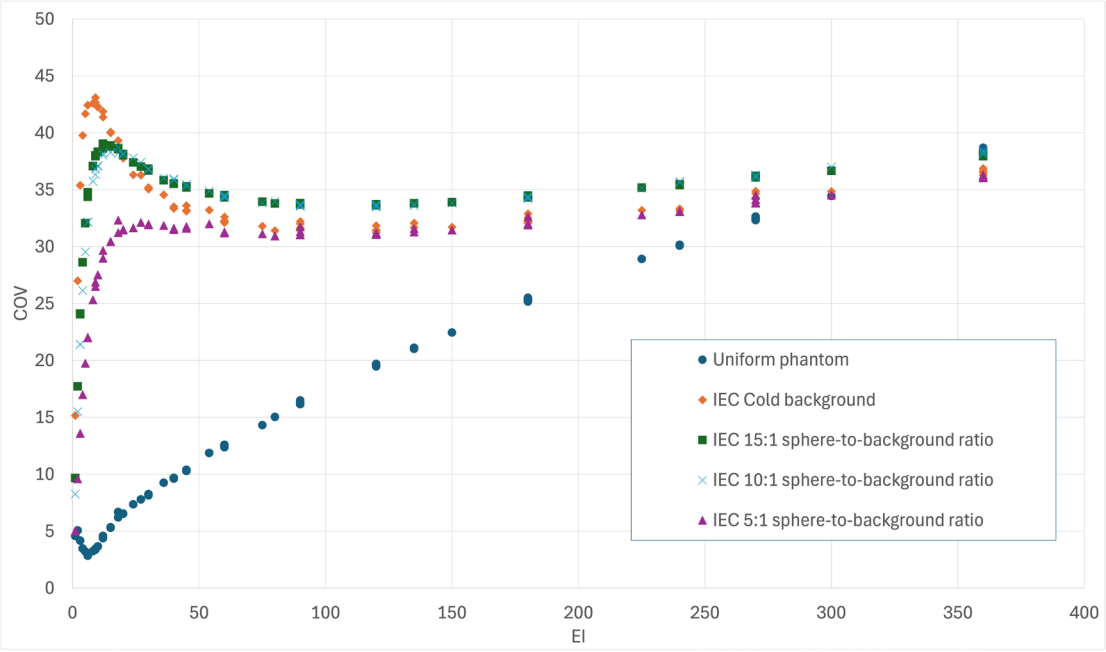

Figure 2. Coefficient of variation (COV) as a function of equivalent iterations (EI) for the Symbia Pro.specta system. Results are shown for the uniform phantom and for the largest sphere of the IEC NEMA body phantom under different sphere-to-background activity concentration ratios (cold background, 15:1, 10:1, and 5:1). The COV exhibits a clear dependence on EI, with consistent behavior across different acquisition conditions.

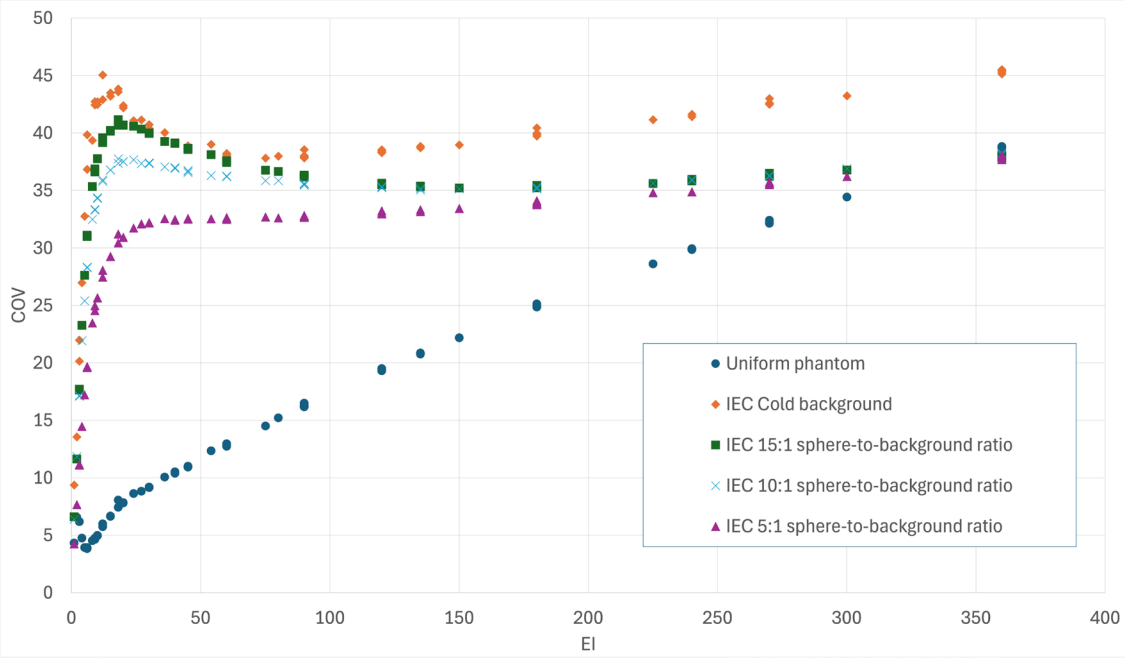

Figure 3. Coefficient of variation (COV) as a function of equivalent iterations (EI) for the Symbia Intevo Bold system using the FLASH3D reconstruction algorithm. Results are shown for the uniform phantom and for the largest sphere of the IEC NEMA body phantom under different sphere-to-background ratios (cold background, 15:1, 10:1, and 5:1). The overall behavior is consistent with that observed for the Symbia Pro.specta system, with slightly higher absolute noise levels.

A markedly different behavior was observed for the quantitative xSPECT Quant algorithm. In this case, higher noise levels were obtained compared to OSEM-based reconstructions. Due to the increased noise, only a limited range of subsets was investigated. Unlike the OSEM-based algorithms, the COV was no longer solely determined by EI. Instead, different combinations of subsets and iterations corresponding to the same EI produced substantially different COV values, as shown in Figure 4. For example, in the uniform phantom at EI = 60, the combinations 1 subset × 60 iterations, 2 subsets × 30 iterations, and 4 subsets × 15 iterations resulted in COV values of 23%, 31%, and 32%, respectively.

This behavior indicated that, for xSPECT Quant, image noise depended explicitly on the individual reconstruction parameters rather than on their product, reflecting the fundamental differences between the OSCG algorithm and conventional OSEM-based approaches.

Consistently, for identical reconstruction settings, the COV values obtained with xSPECT Quant were substantially higher than those obtained with FLASH3D and FLASH3D+, in agreement with previous findings.[40] For example, for two subsets and 30 iterations, COV values of approximately 12% and 13% were obtained for FLASH3D+ and FLASH3D, respectively, compared to 31% for xSPECT Quant.

In the IEC NEMA phantom, only the lowest subset values (1 and 2) were analyzed due to noise considerations. The general trend of the COV as a function of EI was similar to that observed for OSEM-based algorithms, with an initial local maximum at EI ≈ 10–20, followed by a local minimum at EI ≈ 60–90, after which the COV increased monotonically. An exception was observed for the 5:1 sphere-to-background ratio, where the COV exhibited a monotonic increase with EI without clear local extrema.

3.2. Conversion factor analysis

The conversion factor was calculated for the non-quantitative reconstruction algorithms FLASH3D and FLASH3D+. For each algorithm, the conversion factor was evaluated for all combinations of subsets and iterations considered in the reconstruction process.

The analysis showed that, similarly to the COV, the conversion factor depended on the product of subsets and iterations, i.e., on the number of EI, for both reconstruction algorithms.

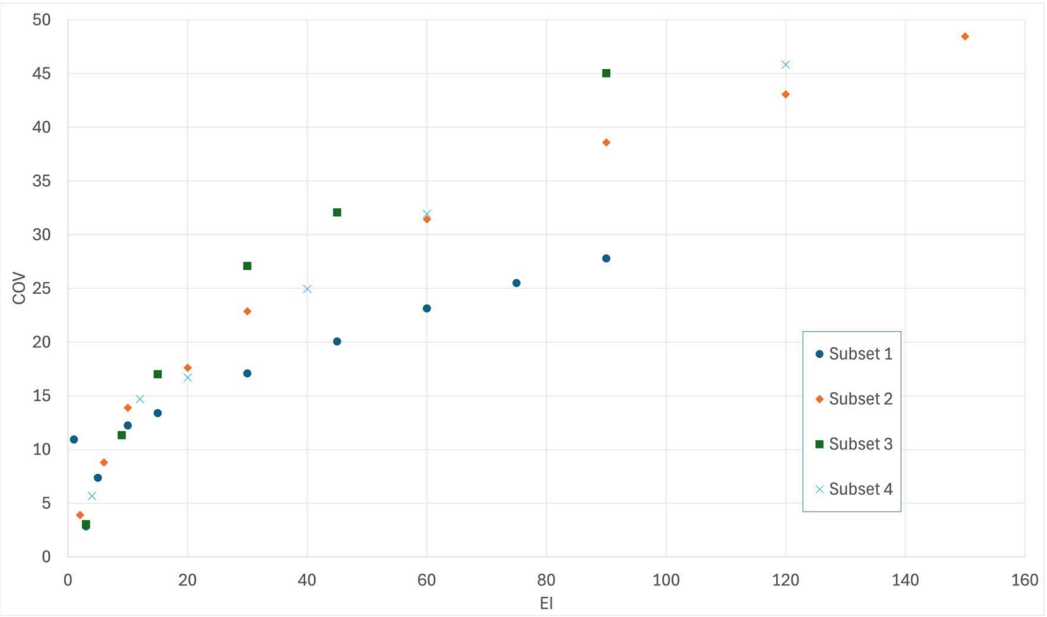

Figure 4. Coefficient of variation (COV) as a function of equivalent iterations (EI) for the Symbia Intevo Bold system using the xSPECT Quant reconstruction algorithm. Results are shown for the uniform phantom for subsets 1, 2, 3, and 4. Unlike ordered-subset expectation maximization-based reconstructions, the COV does not depend uniquely on EI, and different combinations of subsets and iterations lead to significantly different noise levels.

Figure 5 shows the trend of the conversion factor as a function of EI for both algorithms: (A) FLASH3D+ and (B) FLASH3D. A similar behavior was observed in both cases: the conversion factor exhibited a steep increase at low EI values, corresponding to an unstable reconstruction regime, followed by a maximum around EI ≈ 12–15. For higher EI values, the conversion factor progressively stabilized and reached a plateau.

In particular, the asymptotic conversion factor values were found to be in the range of 20.8–20.9 for FLASH3D+ and 21.6–21.7 for FLASH3D.

In addition to the uniform phantom, the conversion factor was also evaluated using the largest sphere of the IEC NEMA phantom. This analysis was performed for exploratory purposes, in analogy with the evaluation carried out for the COV, in order to better understand the behavior of the conversion factor under non-uniform activity distributions. However, for clinical applications, the conversion factor derived from the uniform phantom was adopted.

The conversion factor trend as a function of EI for the IEC NEMA phantom showed a behavior similar to that observed in the uniform phantom, although without a distinct maximum. Specifically, the conversion factor rapidly increased at low EI values and then gradually stabilized toward a plateau value, which was consistent with that obtained from the uniform phantom.

This behavior was consistently observed for both reconstruction algorithms and for all sphere-to-background activity concentration ratios investigated. Figure 6 shows an example of the conversion factor trend as a function of EI for the FLASH3D+ reconstruction algorithm with a sphere-to-background ratio of 10:1. Only this case is reported, as the behavior was found to be similar across all other configurations.

3.3. Recovery coefficient analysis

The RC is a key parameter in quantitative SPECT imaging, as it accounts for partial volume effects and reconstruction-dependent biases in activity estimation. Its evaluation is therefore essential for optimizing reconstruction protocols and accurately quantifying lesion activity. All three reconstruction algorithms showed a very similar behavior of the RC as a function of the EI for a fixed number of subsets. In all cases, the RC started from low values, approximately 0.2 at low EI, and progressively increased as the number of iterations (and thus EI) increased, eventually converging toward a plateau value.

For all reconstruction algorithms, the convergence value of the RC was strongly dependent on the sphere size. In particular, the largest sphere exhibited the highest RC values, while smaller spheres showed progressively lower convergence values. This behavior reflected the increasing impact of partial volume effects with decreasing lesion size.

For a sphere-to-background activity concentration ratio of 10:1, the asymptotic RC values for the largest sphere were found to be approximately 0.9 for the FLASH3D+ algorithm (Symbia Pro.specta), about 0.94 for the FLASH3D algorithm (Symbia Intevo Bold), and close to 1 for the quantitative xSPECT Quant reconstruction (Symbia Intevo Bold). Although these values slightly varied for different sphere-to-background activity concentration ratios, the same relative behavior between reconstruction algorithms was consistently observed. The influence of the activity concentration ratio was discussed later in this section. Figure 7 shows a representative example of the RC as a function of EI (subset = 2) for different sphere sizes using the FLASH3D+ reconstruction algorithm for a sphere-to-background activity concentration ratio of 10:1. Similar trends were observed for the other reconstruction algorithms.

The influence of the reconstruction algorithm on the RC was evaluated by comparing the RC as a function of the EI for different reconstruction methods. The results showed that the overall trend of the RC as a function of EI remained substantially unchanged when the reconstruction algorithm varied. In all cases, the RC increased at low EI values and progressively converged toward a plateau as the number of iterations increased. The main difference between the reconstruction algorithms was observed in the asymptotic value reached at convergence. For all subset values, sphere sizes, and sphere-to-background activity concentration ratios, the highest plateau values were consistently obtained with the xSPECT Quant algorithm, with RC values approaching unity. This was followed by the FLASH3D algorithm, while the lowest RC values were observed for the FLASH3D+ reconstruction. Figure 8 shows a representative example of the RC as a function of EI for the largest sphere, using a fixed number of subsets (subset = 2) and a sphere-to-background activity concentration ratio of 10:1. The curves corresponding to FLASH3D, FLASH3D+, and xSPECT Quant were reported. Similar convergence behavior and different plateau values among the algorithms were clearly visible. Similar trends were observed for other reconstruction settings.

The influence of the sphere-to-background activity concentration ratio on the RC was investigated for all three reconstruction algorithms. For all reconstruction methods, the highest RC values were observed in the cold background configuration, where no activity was present in the background. In this case, the RC curve lay systematically

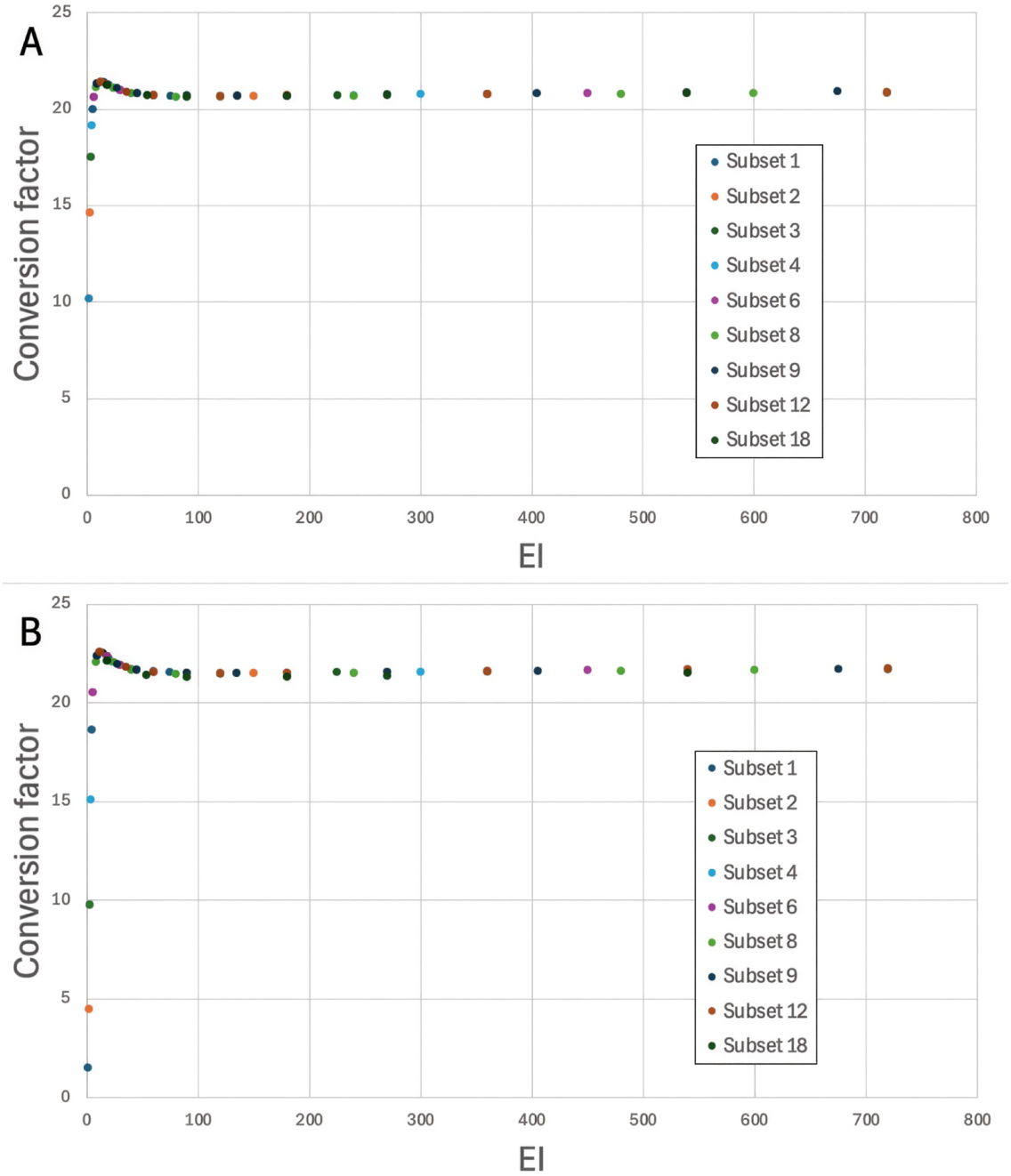

Figure 5. Conversion factor as a function of the equivalent iteration (EI) value for both reconstruction algorithms: (A) FLASH3D+ and (B) FLASH3D. Different curves correspond to different subset values used in the reconstruction, highlighted with distinct colors. Despite the use of different subsets, the results show that the conversion factor depends primarily on the product of subsets and iterations rather than on the individual reconstruction parameters.

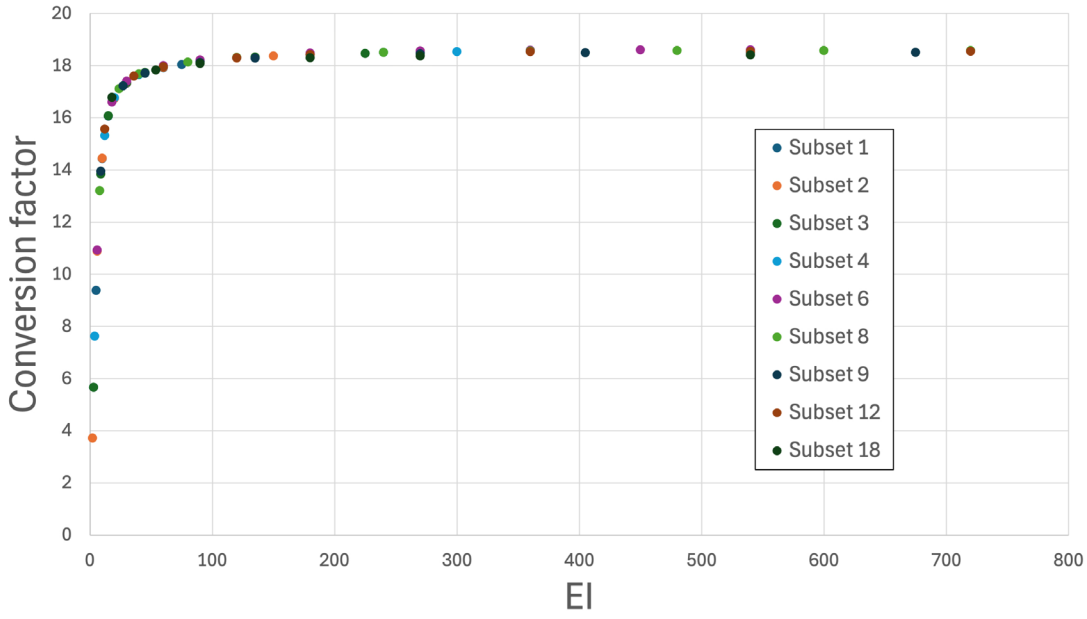

Figure 6. Conversion factor (CF) as a function of equivalent iterations for the IEC NEMA phantom using the FLASH3D+ reconstruction algorithm and a sphere-to-background activity concentration ratio of 10:1. Different subset values are represented with different colors. Only one representative case is shown, as similar trends were observed for all sphere-to-background ratios and for both reconstruction algorithms.

above those obtained for hot background conditions. This behavior was expected, as the absence of background activity reduces spill-in and spill-out effects, leading to improved activity recovery. Regarding the asymptotic behavior, the FLASH3D+ algorithm did not reach unity even at convergence, whereas the FLASH3D algorithm approached RC values close to 1. The xSPECT Quant reconstruction, instead, slightly exceeded unity, indicating a small overestimation of the activity concentration. For hot background conditions, three different sphere-to-background activity concentration ratios were considered (15:1, 10:1, and 5:1). For all reconstruction algorithms, the RC values obtained for these ratios were similar, with only minor differences observed. In particular, for the FLASH3D+ algorithm, the 15:1 ratio yielded slightly higher RC values compared to the other ratios, while for FLASH3D and xSPECT Quant, the differences between the considered ratios were negligible. Figure 9 shows the RC as a function of EI for the largest sphere (subset = 2) for FLASH3D+, while Figures 10–11 report the corresponding results for FLASH3D and xSPECT Quant, respectively. In each case, curves corresponding to different sphere-to-background activity concentration ratios, including the cold background configuration, were displayed. The same overall behavior was observed across all reconstruction algorithms.

3.4. Optimization of reconstruction parameters

The reconstruction parameters were optimized by balancing two competing aspects of quantitative SPECT imaging: RC convergence and image noise. Increasing the number of iterations generally improved RC convergence, leading to more accurate activity recovery, particularly for larger lesions. However, higher iteration numbers also produced a progressive increase in image noise, which could compromise image quality and quantitative stability. Conversely, reconstruction settings with excessively low EI resulted in lower noise levels but incomplete RC convergence, leading to an underestimation of the activity concentration. Therefore, selecting optimal reconstruction parameters required identifying a compromise between quantitative accuracy and acceptable noise levels.

Image noise was evaluated through COV analysis performed on the uniform phantom, while quantitative convergence was assessed through the RC analysis described in the previous section. For the non-quantitative reconstruction algorithms (FLASH3D and FLASH3D+), a COV threshold of 15% was considered acceptable for clinical applications. This threshold was adopted from the European Federation of Organizations for Medical Physics guidelines for quality control in positron emission tomography/CT and PET/magnetic resonance systems

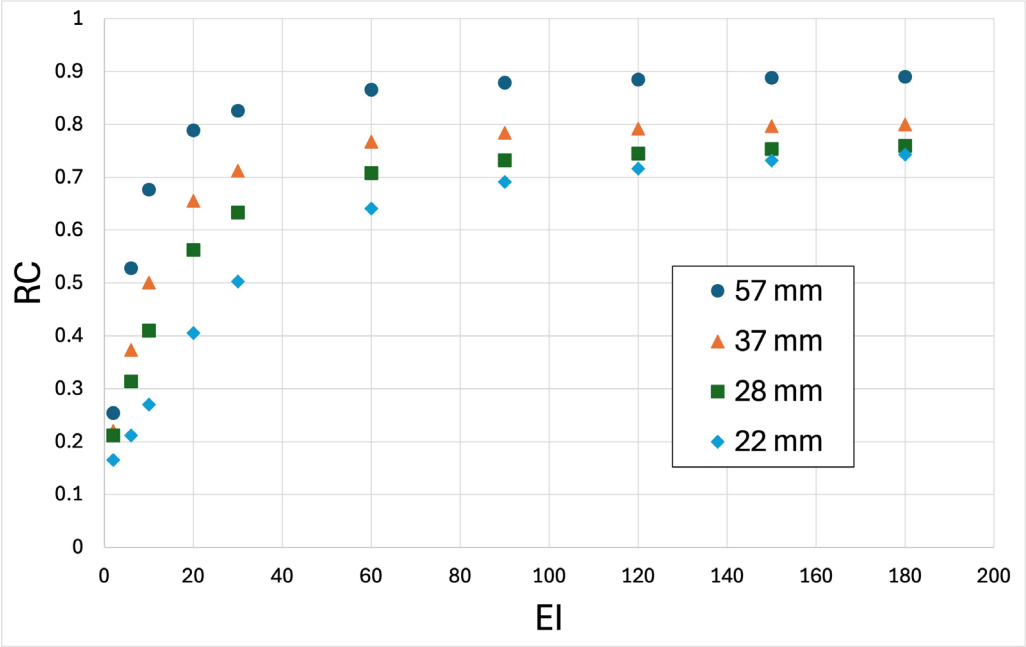

Figure 7. Recovery coefficient (RC) as a function of equivalent iterations (EI) (with subset = 2) for the first four sphere sizes (diameter of 57 mm, 37 mm, 28 mm, and 22 mm) of the IEC NEMA phantom using the FLASH3D+ reconstruction algorithm. Each curve corresponds to a different sphere diameter. The RC increases with EI and reaches a plateau, with higher values observed for larger spheres due to reduced partial volume effects. Similar trends were observed for the other reconstruction algorithms.

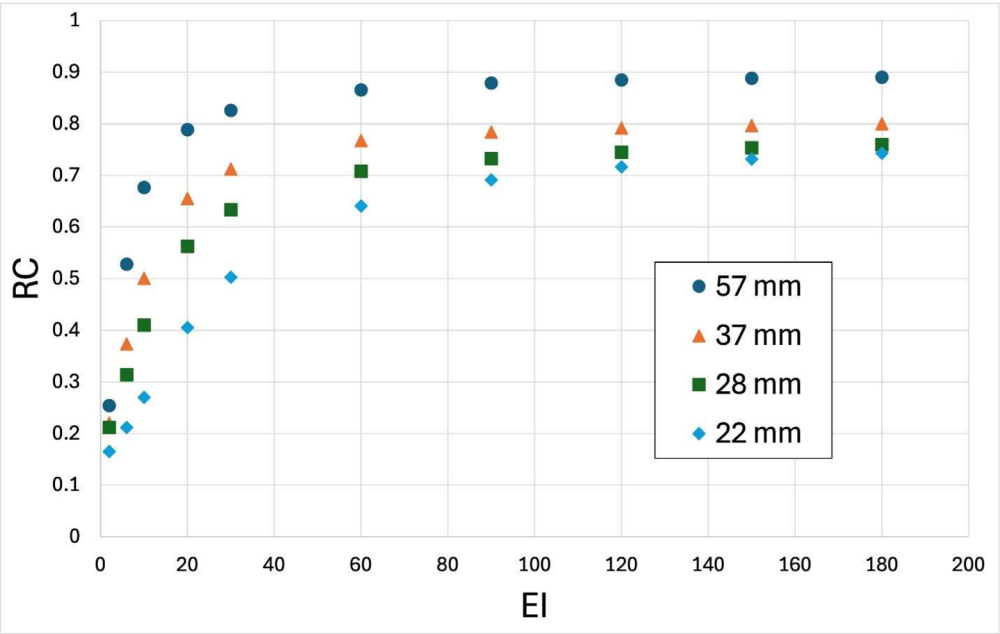

Figure 8. Recovery coefficient (RC) as a function of equivalent iterations (EI) for the largest sphere of the IEC NEMA phantom, using subset = 2 and a sphere-to-background activity concentration ratio of 10:1. Curves corresponding to different reconstruction algorithms (FLASH3D, FLASH3D+, and xSPECT Quant) are shown. While the convergence behavior is similar for all algorithms, different plateau values are observed, with xSPECT Quant providing the highest RC values, followed by FLASH3D and FLASH3D+.

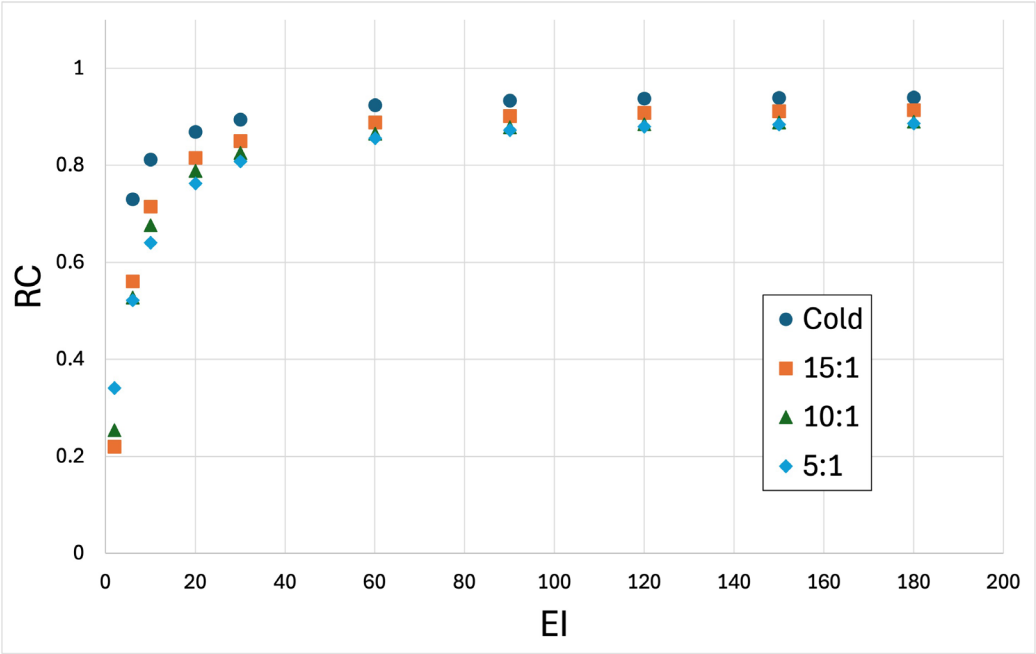

Figure 9. Recovery coefficient (RC) as a function of equivalent iterations (EI) for the largest sphere of the IEC NEMA phantom (subset = 2) using the FLASH3D+ reconstruction algorithm. Results are shown for different sphere-to-background activity concentration ratios (15:1, 10:1, 5:1, and cold background). The cold background configuration consistently provides higher RC values, while only minor differences are observed among the hot background ratios.

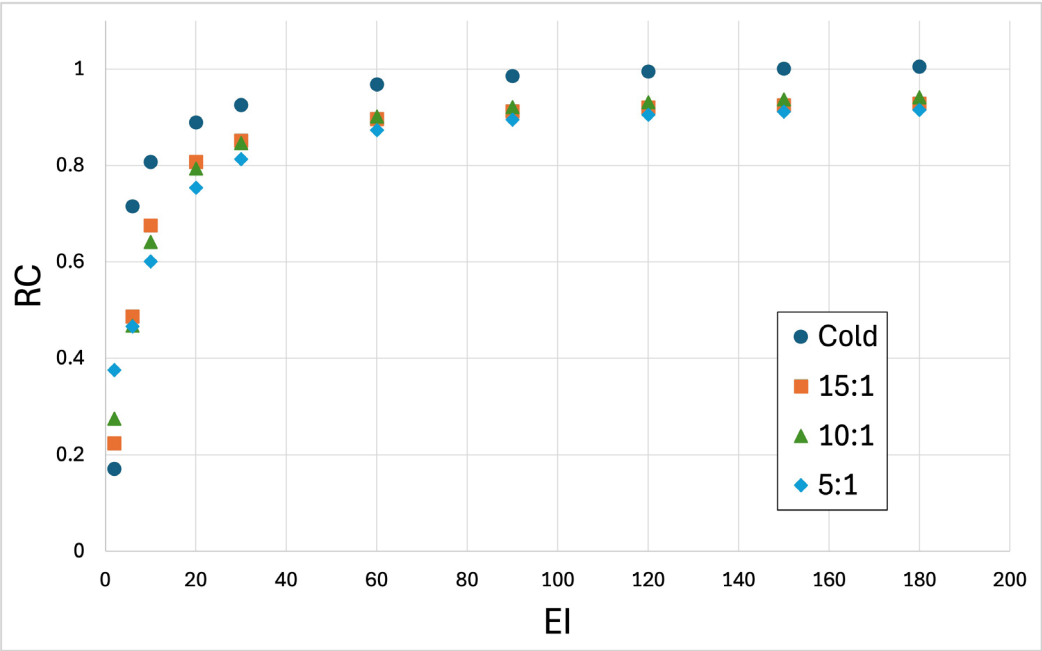

Figure 10. Recovery coefficient (RC) as a function of equivalent iterations (EI) for the largest sphere of the IEC NEMA phantom (subset = 2) using the FLASH3D reconstruction algorithm. Results are shown for different sphere-to-background activity concentration ratios (15:1, 10:1, 5:1, and cold background). The cold background configuration consistently provides higher RC values, while only minor differences are observed among the hot background ratios.

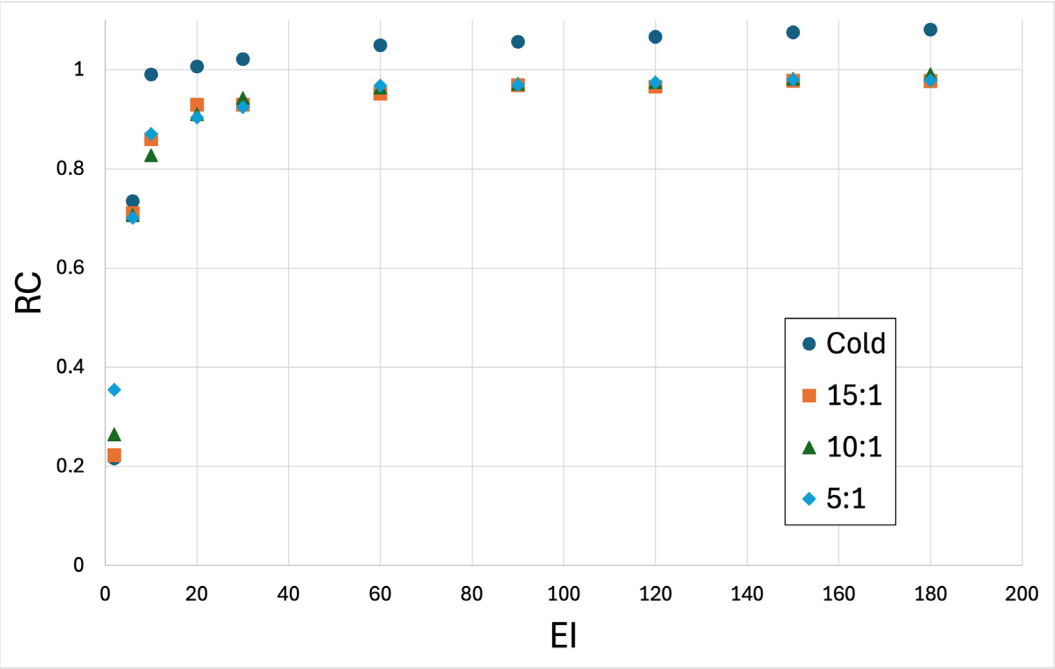

Figure 11. Recovery coefficient (RC) as a function of equivalent iterations (EI) for the largest sphere of the IEC NEMA phantom (subset = 2) using the xSPECT Quant reconstruction algorithm. Results are shown for different sphere-to-background activity concentration ratios (15:1, 10:1, 5:1, and cold background). The cold background configuration consistently provides higher RC values, while only minor differences are observed among the hot background ratios.

and was used in this study as a reference criterion for SPECT/CT imaging.[43] Among the reconstruction settings satisfying this condition, the configuration providing RC values closest to unity was selected.

Based on this optimization procedure, the reconstruction parameters corresponding to 2 subsets and 30 iterations were identified as the optimal compromise between noise and quantitative convergence for the non-quantitative protocols. These parameters allowed the RC curves to approach convergence while maintaining COV values within the predefined acceptable range.

For the quantitative xSPECT Quant reconstruction, the same reconstruction settings (2 subsets and 30 iterations) were adopted. This choice ensured consistency across all reconstruction protocols and simplified subsequent clinical implementation and comparison of the reconstruction methods. Although the COV measured for xSPECT Quant under these conditions was higher (approximately 31%), the noise level was still considered acceptable.

For all reconstruction protocols, the Gaussian post-reconstruction filter was set to 0 mm in order to avoid additional smoothing effects that could alter the quantitative evaluation and RC measurements.

The selected reconstruction parameters therefore represent the reconstruction settings adopted for clinical quantitative imaging of patients treated with ^{177}Lu radiopharmaceuticals. Consequently, the quantification validation and calibration uncertainty estimation presented in the following sections were performed using these optimized reconstruction settings.

3.5. Recovery coefficient fitting

For clinical implementation, the RC cannot be directly derived only from the discrete experimental points obtained from the IEC NEMA phantom spheres. In clinical practice, lesions may present arbitrary sizes and shapes that do not exactly correspond to the phantom inserts. Therefore, a continuous mathematical model describing the RC behavior is required in order to associate each lesion with an appropriate RC.

For this purpose, only the reconstruction settings previously identified as optimal (two subsets and 30 iterations) were considered. All reconstruction algorithms and sphere-to-background activity concentration ratios were analyzed under these conditions. The IEC NEMA phantom consisted of the six standard IEC NEMA spheres together with an additional custom-made larger

sphere with a volume of approximately 97 mL. Overall, a total of 12 datasets were analyzed, corresponding to three reconstruction algorithms (FLASH3D, FLASH3D+, and xSPECT Quant) and four sphere-to-background configurations (cold background, 5:1, 10:1, and 15:1).

The RC was expressed as a function of the volume-to-surface ratio (V/S) of the inserts rather than only their volume. This choice was motivated by the fact that the RC was influenced not only by lesion volume but also by lesion shape and surface extension. In particular, two inserts having the same volume but different geometrical shapes, and therefore different surface areas, may exhibit different RC values. Inserts characterized by larger surfaces generally present lower RC values due to the increased contribution of spill-in and spill-out effects at the lesion boundaries. Another factor affecting the RC was the spatial resolution of the imaging system, commonly described through the full width at half maximum (FWHM) of a point source response.

This approach was based on the RC model proposed in the MIRD Pamphlet No. 32,[28] in which the RC was described as a function of both the V/S and the spatial resolution of the imaging system. Following the methodology suggested in the pamphlet, the experimental RC data were fitted using a three-parameter logistic function of the form:

$$RC = 1 - \frac{1}{\left(1 + \left(\frac{V/S}{\beta \cdot FWHM}\right)^{\gamma}\right)^{L}} \tag{7}$$

where β, γ, and L are fitting parameters.

Since each RC curve consisted of only seven experimental points, the use of a three-parameter model allowed a sufficiently flexible fitting while reducing the risk of overfitting.

The spatial resolution of the FLASH3D+ and FLASH3D reconstruction algorithms was evaluated according to the NEMA NU 2 standard, yielding an average FWHM of approximately 0.55 cm in all three spatial directions. This value was therefore adopted for all fitting procedures involving these reconstruction methods.

In contrast, the spatial resolution of the xSPECT Quant reconstruction could not be rigorously defined according to the NEMA methodology. This was due to the reconstruction protocol's intrinsic characteristics, which required CT-based attenuation correction and did not permit reconstruction without attenuation correction, as required by the standard NEMA protocol.

Consequently, a direct NEMA-based estimation of the spatial resolution was not feasible for this reconstruction method. For this reason, no experimentally derived FWHM value was assigned to xSPECT Quant. However, for the purposes of the fitting procedures, a conservative assumption was made. Considering that the voxel size of the xSPECT Quant reconstruction was larger than that used in the OSEM-based reconstructions, and to ensure a conservative approach, a spatial resolution value of 1 cm (FWHM) was adopted.

The fitting procedure was implemented using an in-house Python script. The optimized fitting parameters obtained for each reconstruction algorithm and activity concentration ratio were stored and subsequently used in clinical routine. In practical applications, the lesion or organ surface and volume were measured from the segmented structure, the most appropriate lesion-to-background activity concentration ratio was selected, and the reconstruction algorithm used for image reconstruction was identified. The corresponding fitting parameters were then applied to the logistic model in order to estimate the appropriate RC value for that specific lesion.

Figure 12 shows representative examples of RC curves as a function of the V/S and FWHM, together with the corresponding fitted logistic functions using the optimized parameters. In particular, Figure 12A refers to the FLASH3D reconstruction on the Symbia Intevo Bold system with cold background, while Figure 12B corresponds to the FLASH3D+ reconstruction on the Symbia Pro.specta system with cold background.

3.6. Quantification validation

Validation was performed by comparing the reconstructed activity concentrations within the three anthropomorphic phantom inserts with their corresponding nominal values. For FLASH3D and FLASH3D+, total counts were measured within each segmented VOI, converted into activity using the CF derived from the uniform phantom, and subsequently corrected using the corresponding RC obtained from the fitted model. The appropriate RC was selected according to the sphere-to-background activity concentration ratio for each insert: a cold background for the sphere and a 10:1 background-to-insert activity concentration ratio for the kidney and heart inserts. For xSPECT Quant, reconstructed activity concentrations were directly obtained from the quantitative reconstruction, and only the corresponding RC correction was applied. Surface and volume measurements required for RC estimation were obtained from CT segmentation.

Table 1 summarizes the relative quantification errors obtained for the three inserts using the optimized reconstruction settings. Overall, close agreement was observed between the reconstructed and nominal activity

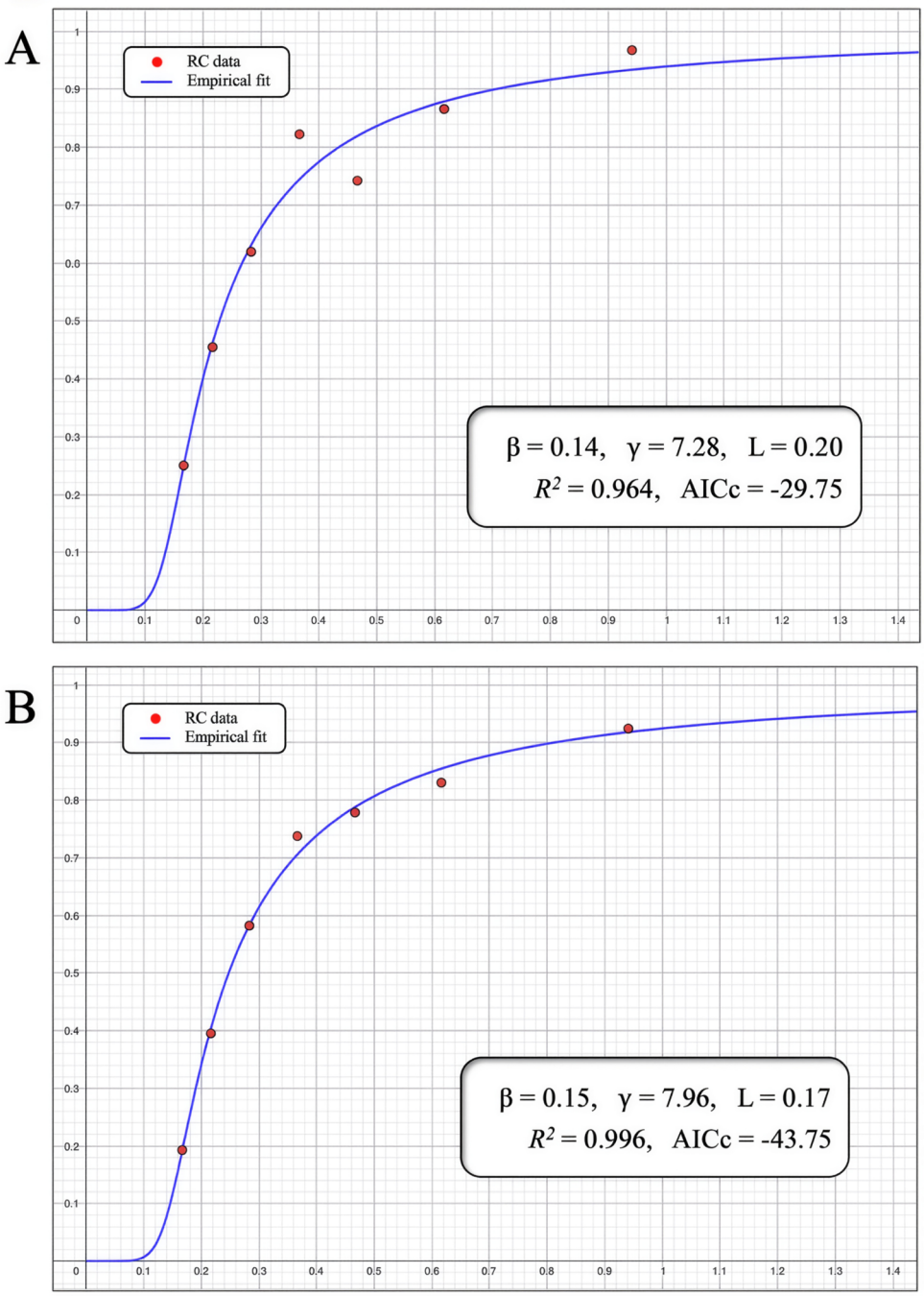

Figure 12. Examples of RC curves as a function of $\left(\frac{V/S}{FWHM}\right)$ together with the corresponding three-parameter logistic fits for (A) FLASH3D on Symbia Intevo Bold and (B) FLASH3D+ on Symbia Pro.specta, both with cold background. The optimized fitting parameters β, γ, and L, as well as the corresponding R^2 and AICc values, are reported in each panel.
Abbreviations: β: Beta; γ: Gamma; AICc: Corrected Akaike information criterion; FWHM: Full width at half maximum; R^2: Coefficient of determination; RC: Recovery coefficient; V/S: Volume-to-surface ratio.

concentrations across all reconstruction algorithms. Among the evaluated methods, xSPECT Quant consistently provided the lowest quantification errors for the sphere and kidney inserts, confirming its superior quantitative recovery performance. For the heart insert, both FLASH3D+ and xSPECT Quant showed a slight overestimation of activity concentration. This behavior was likely related to the complex geometry of the insert and its relatively low V/S, which was associated with a lower RC and therefore a larger correction factor applied to the reconstructed activity concentration.

The observed differences between reconstruction methods were consistent with the RC analysis presented previously. The higher RC values achieved by xSPECT Quant reduced the magnitude of the recovery correction and improved overall quantification accuracy, whereas the lower RC values associated with FLASH3D and FLASH3D+ required larger correction factors and therefore increased sensitivity to uncertainties related to segmentation, calibration, and RC modeling.

These results confirmed the validity of the proposed calibration and correction workflow and supported the use of the optimized reconstruction settings for quantitative ^{177}Lu SPECT/CT imaging in clinical practice.

4. Discussion

The results presented in this work demonstrate that quantitative SPECT/CT imaging for ^{177}Lu is strongly dependent on both the imaging system and the reconstruction methodology adopted. The reconstruction algorithm, reconstruction parameters, calibration strategy, and recovery correction procedure all contributed significantly to the final quantitative accuracy. Consequently, quantitative SPECT cannot be considered a purely acquisition-dependent process, but rather the result of a complex interaction between physical, statistical, and reconstruction-related factors that must be carefully optimized for each clinical implementation.

Image noise behavior was one of the most relevant findings concerning the relationship between reconstruction parameters and image noise. The COV analysis showed that the OSEM-based reconstruction algorithms, namely FLASH3D and FLASH3D+, exhibited a relatively stable and predictable behavior, in which image noise was primarily governed by the number of EI. Different combinations of subsets and iterations that produced the same EI yielded comparable COV values, indicating that, for these algorithms, convergence and noise behavior could be effectively characterized by a single parameter.

In contrast, the quantitative xSPECT Quant reconstruction showed a markedly different behavior. In this case, image noise depended explicitly on the individual reconstruction parameters rather than solely on their product. Different combinations of subsets and iterations corresponding to the same EI produced substantially different COV values, reflecting the fundamentally different statistical framework of the OSCG reconstruction algorithm, alongside any hardware-specific noise characteristics of the Symbia Intevo Bold, compared with conventional OSEM-based methods. These findings confirmed that reconstruction optimization strategies developed for OSEM algorithms could not be directly transferred to xSPECT Quant and that quantitative protocols must therefore be optimized separately for each clinical workflow.

The CF analysis further emphasized the importance of reconstruction convergence for quantitative imaging. For both FLASH3D and FLASH3D+, the CF exhibited unstable behavior at low EI values, characterized by rapid variations during the early reconstruction iterations. Only after sufficient convergence was reached did the CF progressively stabilize toward a plateau region. This behavior indicated that quantitative calibration was reliable only when reconstruction parameters allowed the system to operate within a stable convergence regime. Reconstructions performed with insufficient iterations may therefore lead to systematic inaccuracies in activity estimation, even when all other calibration procedures are correctly implemented.

Interestingly, the behavior of the CF closely mirrored the behavior observed for the COV. Both parameters demonstrated a strong dependence on EI and progressively stabilized at higher iteration numbers. This further supported the interpretation that image convergence and quantitative calibration were intrinsically linked processes in iterative SPECT reconstruction.

Table 1. Relative quantification errors obtained for the three inserts of the anthropomorphic phantom using the optimized reconstruction parameters (two subsets and 30 iterations)

Insert	FLASH3D+	FLASH3D	xSPECT Quant
Sphere insert	−16%	−14%	−6%
Kidney insert	−14%	−16%	−10%
Heart insert	+3%	−8%	+3%

The RC analysis confirmed the major role of partial volume effects in quantitative SPECT imaging. As expected, smaller inserts systematically showed lower RC values due to the limited spatial resolution of the imaging systems and the resulting spill-out effects. Conversely, larger spheres exhibited RC values approaching unity, particularly for highly convergent reconstructions.

The influence of the specific scanner–reconstruction combination was also clearly evident. Among the investigated scanner–reconstruction combinations, the xSPECT Quant workflow yielded the highest RC values. The standard FLASH3D workflow showed intermediate behavior, while the FLASH3D+ workflow systematically produced lower RC values. These differences were likely associated with the distinct reconstruction models adopted by the software (including differences in resolution recovery implementation, convergence properties, and quantitative corrections) as well as the inherent hardware differences between the Symbia Intevo Bold and Symbia Pro.specta scanners used for the acquisitions.

The influence of background activity was comparatively smaller. Although the cold background configuration yielded slightly higher RC values, only modest differences were observed among the hot background ratios investigated (15:1, 10:1, and 5:1). This suggested that, within the investigated range, lesion size and the chosen clinical workflow were the dominant factors affecting quantitative recovery.

The optimization strategy adopted in this study was based on jointly evaluating quantitative accuracy and image noise. For FLASH3D and FLASH3D+, the reconstruction parameters were selected from configurations that achieved a COV below the reference threshold of 15%, with the configuration yielding RCs closest to unity being selected. This approach identified the combination of two subsets and 30 iterations as the most suitable compromise between quantitative convergence and image noise. For xSPECT Quant, the same reconstruction settings were intentionally retained to ensure methodological consistency across all reconstruction protocols and to facilitate their comparison and subsequent clinical implementation. Although the corresponding COV (approximately 31%) exceeded the reference threshold adopted for FLASH3D and FLASH3D+, this higher noise level was consistent with the intrinsic characteristics of xSPECT Quant, which prioritized quantitative accuracy over image smoothing. Consequently, the increased statistical noise was considered an acceptable trade-off given the algorithm's improved quantitative performance and the practical difficulty of achieving substantially lower noise levels without compromising activity recovery.

For the non-quantitative workflows, these parameters ensured COV values below the predefined acceptability threshold while allowing the RC curves to approach their asymptotic behavior. Although the xSPECT Quant configuration produced substantially higher noise levels under the same conditions, the improved quantitative recovery provided by this system–algorithm combination supported the adoption of identical reconstruction settings for all protocols. Maintaining the same reconstruction configuration across all methods also simplified clinical implementation and facilitated comparison between reconstruction strategies.

Validation using the anthropomorphic phantom supported the validity of the proposed calibration workflows. All evaluated scanner–reconstruction combinations provided reconstructed activity concentrations in reasonable agreement with the nominal values, confirming the validity of the calibration procedure and RC correction methodology. Among the investigated methods, the xSPECT Quant workflow achieved the lowest quantification errors for most inserts, consistent with its higher RCs.

The slight overestimation observed for the heart insert in some reconstructions was likely related to the insert's complex geometry and its relatively low V/S. Since structures characterized by low RC values required larger correction factors, uncertainties associated with segmentation, RC fitting, and calibration were amplified, thereby increasing the sensitivity of the final activity estimation. This observation further highlighted the importance of accurate recovery correction modeling in non-spherical geometries.

Overall, the present results indicated that accurate quantitative ^{177}Lu SPECT/CT imaging depended on careful optimization of reconstruction parameters, calibration methodology, and recovery correction. Within the specific scanner–reconstruction combinations evaluated in this study, the xSPECT Quant workflow yielded higher RCs and lower quantification errors, whereas the evaluated OSEM-based workflows produced lower image noise but reduced activity recovery. Because these findings were derived from different hardware platforms, they should be interpreted as specific to the investigated clinical workflows and not as a direct comparison of reconstruction algorithms. Nevertheless, the proposed calibration and validation workflow provide a practical framework for the local commissioning of quantitative ^{177}Lu SPECT/CT systems intended for patient-specific dosimetry.

A primary limitation of this study was the inherent confounding factor introduced during the evaluation of the reconstruction algorithms across two different SPECT/

CT hardware platforms. Specifically, xSPECT Quant and standard FLASH3D were evaluated on the Symbia Intevo Bold, whereas FLASH3D+ was evaluated on the Symbia Pro.specta system. Consequently, any observed differences in quantitative accuracy, RCs, or image noise reflected the overall performance of the specific scanner–reconstruction combination rather than isolated differences in the software algorithms alone. Variations in detector electronics, collimator manufacturing tolerances, or system geometry between the two scanners could contribute to the measured outcomes. Therefore, our findings should be strictly interpreted as an evaluation of these distinct clinical workflows, rather than a pure algorithmic comparison.

5. Conclusion

This work presented a practical commissioning and optimization workflow for quantitative ^{177}Lu SPECT/CT imaging using two commercial Siemens SPECT/CT platforms. The proposed methodology combined image noise characterization, CF determination, RC modeling, reconstruction parameter selection, and anthropomorphic phantom validation to support reliable activity quantification within the investigated clinical workflows.

The results indicated that quantitative performance depended on both the scanner platform and the reconstruction methodology adopted. The evaluated OSEM-based workflows showed predictable convergence behavior and lower image noise, whereas the xSPECT Quant workflow yielded higher RCs and lower quantification errors, albeit with increased image noise. Because the investigated reconstruction methods were implemented on different hardware platforms, these findings should be interpreted as reflecting the performance of the specific scanner–reconstruction combinations rather than the intrinsic superiority of one reconstruction algorithm over another.

Within the investigated parameter space, the combination of two subsets and 30 iterations provided the most favorable trade-off between quantitative accuracy and image noise. Specifically, this reconstruction setting yielded RCs closest to unity while maintaining the COV below the predefined acceptance threshold of 15%, and was therefore selected for the subsequent quantitative analyses.

Overall, the proposed calibration and optimization procedure provides a practical framework for the local commissioning and validation of quantitative ^{177}Lu SPECT/CT systems intended to support patient-specific dosimetry and radionuclide therapy monitoring. Future work should include validation on larger clinical cohorts, evaluation across additional reconstruction platforms, and further investigation of automated segmentation and artificial intelligence–based approaches.

Acknowledgments

None.

Funding

None.

Conflict of interest

The authors declare they have no competing interests.

Author contributions

Conceptualization: Leonardo Lampertico, Gaia Muti
Investigation: Leonardo Lampertico
Methodology: Leonardo Lampertico, Gaia Muti, Claudia Carbonini, Chiara Romanò
Resources: Claudio Rossetti, Antonio Scarale
Supervision: Paola Enrica Colombo
Writing–original draft: Leonardo Lampertico
Writing–review & editing: Leonardo Lampertico, Gaia Muti

Ethics approval and consent to participate

Not applicable.

Consent for publication

Not applicable.

Availability of data

Data are available from the corresponding author upon reasonable request.

References

1. Dash A, Knapp FF, Pillai MRA. Targeted radionuclide therapy - an overview. *Curr Radiopharm*. 2013;6(3):152-180.

   doi: 10.2174/18744710113066660023

2. Baum RP, Kulkarni HR. THERANOSTICS: from molecular imaging using Ga-68 labeled tracers and PET/CT to personalized radionuclide therapy - the Bad Berka experience. *Theranostics*. 2012;2(5):437-447.

   doi: 10.7150/thno.3645

3. Dash A, Chakraborty S, Pillai MR, Knapp FF Jr. Peptide receptor radionuclide therapy: an overview. *Cancer Biother Radiopharm*. 2015;30(2):47-71.

   doi: 10.1089/cbr.2014.1741

4. Herrmann K, Schwaiger M, Lewis JS, *et al*. Radiotheranostics: a roadmap for future development. *Lancet Oncol*. 2020;21(3):e146-e156.

   doi: 10.1016/S1470-2045(19)30821-6

5. Otte A, Müller-Brand J, Dellas S, Nitzsche EU, Herrmann R, Maecke HR. Yttrium-90-labelled somatostatin-analogue for cancer treatment. *Lancet*. 1998;351(9100):417-418.

doi: 10.1016/S0140-6736(05)78355-0

6. Kwekkeboom DJ, de Herder WW, Kam BL, *et al.* Treatment with the radiolabeled somatostatin analog [^{177}Lu-DOTA^{0},Tyr^{3}]octreotate: toxicity, efficacy, and survival. *J Clin Oncol*. 2008;26(13):2124-2130.

doi: 10.1200/JCO.2007.15.2553

7. Römer A, Seiler D, Marincek N, *et al.* Somatostatin-based radiopeptide therapy with [^{177}Lu-DOTA]-TOC versus [^{90}Y-DOTA]-TOC in neuroendocrine tumours. *Eur J Nucl Med Mol Imaging*. 2014;41(2):214-222.

doi: 10.1007/s00259-013-2559-8

8. Paganelli G, Sansovini M, Ambrosetti A, *et al.* 177Lu-Dota-octreotate radionuclide therapy of advanced gastrointestinal neuroendocrine tumors: results from a phase II study. *Eur J Nucl Med Mol Imaging*. 2014;41(10):1845-1851.

doi: 10.1007/s00259-014-2735-5

9. Strosberg J, El-Haddad G, Wolin E, *et al.* Phase 3 trial of ^{177}Lu-Dotatate for midgut neuroendocrine tumors. *N Engl J Med*. 2017;376(2):125-135.

doi: 10.1056/NEJMoa1607427

10. Strosberg JR, Caplin ME, Kunz PL, *et al.* NETTER-1 investigators. ^{177}Lu-Dotatate plus long-acting octreotide versus high-dose long-acting octreotide in patients with midgut neuroendocrine tumours (NETTER-1): final overall survival and long-term safety results from an open-label, randomised, controlled, phase 3 trial. *Lancet Oncol*. 2021;22(12):1752-1763.

doi: 10.1016/S1470-2045(21)00572-6

11. Benešová M, Schäfer M, Bauder-Wüst U, *et al.* Preclinical evaluation of a tailor-made DOTA-conjugated PSMA inhibitor with optimized linker moiety for imaging and endoradiotherapy of prostate cancer. *J Nucl Med*. 2015;56(6):914-920.

doi: 10.2967/jnumed.114.147413

12. Pillai AM, Knapp FF Jr. Lutetium-177 labeled therapeutics: ^{177}Lu-PSMA is set to redefine prostate cancer treatment. *Curr Radiopharm*. 2016;9(1):6-7.

doi: 10.2174/1874471009011511231248 26

13. Sartor O, de Bono J, Chi KN, *et al.* Lutetium-177-PSMA-617 for metastatic castration-resistant prostate cancer. *N Engl J Med*. 2021;385(12):1091-1103.

doi: 10.1056/NEJMoa2107322

14. Kratochwil C, Fendler WP, Eiber M, *et al.* Joint EANM/SNMMI procedure guideline for the use of ^{177}Lu-labeled PSMA-targeted radioligand-therapy (^{177}Lu-PSMA-RLT). *Eur J Nucl Med Mol Imaging*. 2023;50(9):2830-2845.

doi: 10.1007/s00259-023-06255-8

15. Sgouros G, Hobbs RF. Dosimetry for radiopharmaceutical therapy. *Semin Nucl Med*. 2014;44(3):172-178.

doi: 10.1053/j.semnuclmed.2014.03.007

16. Sjögreen Gleisner K, Chouin N, Gabina PM, *et al.* EANM dosimetry committee recommendations for dosimetry of 177Lu-labelled somatostatin-receptor- and PSMA-targeting ligands. *Eur J Nucl Med Mol Imaging*. 2022;49(6):1778-1809.

doi: 10.1007/s00259-022-05727-7

17. Bolch WE, Eckerman KF, Sgouros G, Thomas SR. MIRD pamphlet No. 21: a generalized schema for radiopharmaceutical dosimetry—standardization of nomenclature. *J Nucl Med*. 2009;50(3):477-484.

doi: 10.2967/jnumed.108.056036

18. Dewaraja YK, Frey EC, Sgouros G, *et al.* MIRD Pamphlet No. 23: Quantitative SPECT for Patient-Specific 3-Dimensional Dosimetry in Internal Radionuclide Therapy. *J Nucl Med*. 2012;53(8):1310-1325.

doi: 10.2967/jnumed.111.100123

19. Ljungberg M, Celler A, Konijnenberg MW, Eckerman KF, Dewaraja YK, Sjögreen-Gleisner K. MIRD Pamphlet No. 26: joint EANM/MIRD guidelines for quantitative ^{177}Lu SPECT applied for dosimetry of radiopharmaceutical therapy. *J Nucl Med*. 2016;57(1):151-162.

doi: 10.2967/jnumed.115.159012

20. Sandström M. *Dosimetry of Radionuclide Therapy with ^{177}Lu-octreotate*. Doctoral dissertation. Uppsala, Sweden: Uppsala University; 2011. Accessed July 30, 2026. http://urn.kb.se/resolve?urn=urn:nbn:se:uu:diva-158973.

21. Sundlöv A, Gleisner KS, Tennvall J, *et al.* Phase II trial demonstrates the efficacy and safety of individualized, dosimetry-based ^{177}Lu-DOTATATE treatment of NET patients. *Eur J Nucl Med Mol Imaging*. 2022;49(11):3830-3840.

doi: 10.1007/s00259-022-05786-w

22. Ljungberg M. Absolute quantitation of SPECT studies. *Semin Nucl Med*. 2018;48(4):348-358.

doi: 10.1053/j.semnuclmed.2018.02.009

23. Bailey DL, Willowson KP. An evidence-based review of quantitative SPECT imaging and potential clinical applications. *J Nucl Med*. 2013;54(1):83-89.

doi: 10.2967/jnumed.112.111476

24. Cherry SR, Sorenson JA, Phelps ME. *Physics in Nuclear Medicine*. 4th ed. Philadelphia: Saunders; 2012.

25. Zeng GL, Galt JR, Wernick MN, Mintzer RA, Aarsvold JN. Single-photon emission computed tomography. In: Wernick MN, Aarsvold JN, eds. *Emission Tomography*. Amsterdam; Boston: Academic Press; 2004:127-152.

doi: 10.1016/B978-012744482-6.50010-7

26. Holm S, Klausen T, Lagerburg V, de Nijs R. Improving quantitative dosimetry in ^{177}Lu-DOTATATE SPECT by energy window-based scatter corrections. *Nucl Med Commun*. 2014;35(5):522-533.

doi: 10.1097/MNM.0000000000000079

27. Zeintl J, Vija AH, Yahil A, Hornegger J, Kuwert T. Quantitative accuracy of clinical ^{99m}Tc SPECT/CT using ordered-subset expectation maximization with 3-dimensional resolution recovery, attenuation, and scatter correction. *J Nucl Med*. 2010;51(6):921-928.

doi: 10.2967/jnumed.109.071571

28. Marquis H, Schmidtlein CR, de Nijs R, *et al.* MIRD pamphlet No. 32: a MIRD recovery coefficient model for resolution characterization and shape-specific partial-volume correction. *J Nucl Med*. 2025;66(3):457-465.

doi: 10.2967/jnumed.124.268520

29. Grings A, Jobic C, Kuwert T, Ritt P. The magnitude of the partial volume effect in SPECT imaging of the kidneys: a phantom study. *EJNMMI Phys*. 2022;9(1):18.

doi: 10.1186/s40658-022-00446-2

30. Ritt P, Vija H, Hornegger J, Kuwert T. Absolute quantification in SPECT. *Eur J Nucl Med Mol Imaging*. 2011;38(S1):69-77.

doi: 10.1007/s00259-011-1770-8

31. Beauregard JM, Hofman MS, Pereira JM, Eu P, Hicks RJ. Quantitative ^{177}Lu SPECT (QSPECT) imaging using a commercially available SPECT/CT system. *Cancer Imaging*. 2011;11(1):56-66.

doi: 10.1102/1470-7330.2011.0012

32. Hippeläinen E, Tenhunen M, Mäenpää H, Sohlberg A. Quantitative accuracy of ^{177}Lu SPECT reconstruction using different compensation methods: phantom and patient studies. *EJNMMI Res*. 2016;6(1):16.

doi: 10.1186/s13550-016-0172-0

33. D'Arienzo M, Cazzato M, Cozzella ML, *et al.* Gamma camera calibration and validation for quantitative SPECT imaging with ^{177}Lu. *Appl Radiat Isot*. 2016;112:156-164.

doi: 10.1016/j.apradiso.2016.03.007

34. Uribe CF, Esquinas PL, Tanguay J, *et al.* Accuracy of ^{177}Lu activity quantification in SPECT imaging: a phantom study. *EJNMMI Phys*. 2017;4(1):2.

doi: 10.1186/s40658-016-0170-3

35. Sanders JC, Kuwert T, Hornegger J, Ritt P. Quantitative SPECT/CT imaging of ^{177}Lu with in vivo validation in patients undergoing peptide receptor radionuclide therapy. *Mol Imaging Biol*. 2015;17(4):585-593.

doi: 10.1007/s11307-014-0806-4

36. Mezzenga E, D'Errico V, D'Arienzo M, *et al.* Quantitative accuracy of ^{177}Lu SPECT imaging for molecular radiotherapy. *PLoS ONE*. 2017;12(8):e0182888.

doi: 10.1371/journal.pone.0182888

37. Raskin S, Gamliel D, Abookasis D, Ben-Haim S, Chicheportiche A. Towards accurate ^{177}Lu SPECT activity quantification and standardization using lesion-to-background voxel ratio. *EJNMMI Phys*. 2023;10(1):5.

doi: 10.1186/s40658-023-00526-x

38. Wevrett J, Fenwick A, Scuffham J, *et al.* Inter-comparison of quantitative imaging of lutetium-177 (^{177}Lu) in European hospitals. *EJNMMI Phys*. 2018;5(1):17.

doi: 10.1186/s40658-018-0213-z

39. Peters SMB, Meyer Viol SL, van der Werf NR, *et al.* Variability in lutetium-177 SPECT quantification between different state-of-the-art SPECT/CT systems. *EJNMMI Phys*. 2020;7(1):9.

doi: 10.1186/s40658-020-0278-3

40. Hoog C, Verrecchia-Ramos E, Dejust S, *et al.* Implementation of xSPECT, xSPECT bone and Broadquant from literature, clinical survey and innovative phantom study with task-based image quality assessment. *Phys Med*. 2023;112:102611.

doi: 10.1016/j.ejmp.2023.102611

41. Tran-Gia J, Lassmann M. Characterization of noise and resolution for quantitative ^{177}Lu SPECT/CT with xSPECT Quant. *J Nucl Med*. 2019;60(1):50-59.

doi: 10.2967/jnumed.118.211094

42. International Electrotechnical Commission. Radionuclide Imaging Devices - Characteristics and Test Conditions - Part 1: Positron Emission Tomographs. IEC 61675-1:2022. International Electrotechnical Commission; 2022. Accessed July 30, 2026. https://webstore.iec.ch/en/publication/67292.

43. European Federation of Organisations for Medical Physics (EFOMP). EFOMP's Guideline: Quality Controls in PET/CT and PET/MR. Version 02.03.2022. 2022. Accessed July 30, 2026. https://www.efomp.org/uploads/10fd24d1-354d-48d6-bf8f-e93e98cb7d81/EFOMP%E2%80%99S%20GUIDELINE%20QUALITY%20CONTROLS%20IN%20PETCT%20AND%20PETMR.pdf